RSC Advances

PAPER

View Article Online
View Journal | View Issue

Cite this: *RSC Adv.*, 2025, **15**, 12797

Carbon dot-mediated synthesis of $NaYF_4$:Yb^{3+},Er^{3+}@carbon dot composites with enhanced upconversion luminescence for temperature sensing†

Linlin Zou,[a] Ting Yu,*[ab] Haoyang Sheng,[a] Yeqing Chen*[a] and Qingguang Zeng*[ab]

Received 6th February 2025
Accepted 16th April 2025

DOI: 10.1039/d5ra00874c

rsc.li/rsc-advances

Upconversion (UC) nanocrystals and carbon dots (CDs) have emerged as significant subjects of research interest across various fields, including biomedicine, fluorescence sensing, and anti-counterfeiting. This study presents a novel method for preparing $NaYF_4$:Yb^{3+},Er^{3+}@CDs composites through the cubic-to-hexagonal phase transformation of $NaYF_4$ mediated by CDs. The formation of these composites was successfully confirmed through morphological and structural analyses. Notably, the composites were found to enhance UC emission and prolong luminescence lifetime, with these effects being dependent on the quantity of CDs used. The experimental results indicate that the enhanced UC emission in the composites is primarily due to the interception of quenching centers, such as hydroxyl (OH^-) groups. Furthermore, these composites with improved UC emission have the potential to serve as highly sensitive optical thermometers based on the fluorescence intensity ratio technique, with optimal green emissions at 298 K and a maximum relative sensitivity of 1.08 K^{-1}. This work paves the way for advancements in UC luminescence and establishes a foundation for the design and fabrication of high-efficiency UC materials with potential applications in optical temperature sensing.

1. Introduction

Lanthanide-doped upconversion (UC) materials, which are capable of absorbing low-energy photons (two or more) and subsequently emitting a photon with higher energy, have garnered considerable research interest due to their potential applications in biomedical imaging, three-dimensional flat panel displays, photonics, and temperature sensing.[1–3] Among UC materials, $NaYF_4$ is a particularly prevalent host lattice, primarily due to its high chemical stability, low phonon energy, and remarkably large band gap.[4–6] Two principal crystal structures are observed in $NaYF_4$: the cubic α-phase, which is metastable at elevated temperatures, and the hexagonal β-phase, which is thermodynamically stable at low temperatures.[7,8] Generally, the cubic α-phase, characterized by its lower formation energy, is initially produced during synthesis and subsequently converted into the β-phase following high-temperature treatment. It has been established that the hexagonal β-phase, owing to its more ordered structure and multi-site characteristics in the hexagonal configuration, exhibits enhanced capabilities as a host lattice for the luminescence of various optically active lanthanide ions. Consequently, significant efforts have been dedicated to elucidating its growth and phase transition mechanisms, with the goal of developing high-efficiency $NaYF_4$ UC materials that demonstrate controllable optical properties to meet current technological demands.[9,10]

Carbon dots (CDs), an emerging fluorescent carbon nanomaterial with a size smaller than 10 nm, have garnered significant attention due to their numerous advantages, including exceptional water solubility, favorable biocompatibility, facile preparation, and unique optical properties.[11–14] It is widely accepted that CDs possess carbonized cores (either crystalline or amorphous) with functionalized surfaces that may contain a variety of functional groups, including carbonyls, carboxylic acids, hydroxyls, epoxides and amines.[15,16] As a result of their diverse surface functional groups and ease of modification, CDs exhibit high effectiveness in surface functionality, thereby considerably broadening the scope of their applications.[17–20] For instance, the presence of active functional groups on the surface of the CDs can help maintain colloidal stability in a wide range of solvents and significantly influence the control of the photoluminescence variation.[21,22]

Recently, significant progress has been made in the field of construction and application of CDs/UC composites.[23–27] The

---

[a] School of Applied Physics and Materials, Wuyi University, Jiangmen, Guangdong 529020, P. R. China. E-mail: yuting1009@163.com; yqchenwyu@126.com; zengqg@mail.ustc.edu.cn

[b] Institute of Carbon Peaking and Carbon Neutralization, Wuyi University, Jiangmen, 529020, P.R. China

† Electronic supplementary information (ESI) available. See DOI: https://doi.org/10.1039/d5ra00874c

integration of CDs with UC materials has been shown to mitigate the aggregation-induced luminescence quenching effect in the solid state for CDs, while simultaneously enhancing existing performance or introducing new functionalities. This process, known as the synergistic effect, extends the range of applications. For example, Li *et al.* proposed a simple solvothermal approach to coat CDs onto the surface of lanthanide-doped UC materials, resulting in a multicolor dual-mode luminescent characteristic that could significantly contribute to the field of anti-counterfeiting.[28] To achieve the desired nanocomposites, Xu *et al.* developed an effective technique for preparing CDs coupled with $NaYF_4$:Yb^{3+},Tm^{3+} nanoparticles (NPs) utilizing silica as an intermediate medium.[29] Due to their remarkable dual-mode luminescent properties, these nanocomposites exhibit immense potential in anti-counterfeiting applications and ion detection, along with cellular imaging capabilities. In addition to developing composites with dual-mode luminescence, considerable efforts have been dedicated to investigating the energy transfer between CDs and UC materials. Notably, Zheng *et al.* proposed a universal approach to achieve near-infrared-excited multicolor afterglow in CDs-based room-temperature afterglow materials through efficient radiative energy transfer.[30] Building on this foundation, a new class of CDs-based composites exhibiting triple-mode luminescence and enhanced chemical stability was developed by incorporating CDs into a Yb^{3+},Tm^{3+}-codoped YF_3 matrix, as documented in a study by the same research group.[31] In light of these fascinating findings, it would be beneficial to broaden the scope of research on CDs/UC composites.

In this study, we employed a hydrothermal method to prepare $NaYF_4$:Yb^{3+},Er^{3+}@CDs composites. Specifically, the synthesis of these composites was successfully achieved through the integration of CDs and UC NPs, facilitated by a cubic-to-hexagonal phase transformation process. We investigated the influence of CDs on the UC emission properties. The results of a systematic microstructural analysis and an examination of the UC emission performance led to the proposal of a potential mechanism for the enhancement of UC emission. Furthermore, we conducted a thorough study on the enhancement of green UC emission, with thermal coupling levels of Er^{3+} serving as a self-calibrated optical thermometry.

2. Experimental procedure

2.1 Materials

Citric acid (≥99.5%), urea (99%), branched polyethylenimine (PEI, 25 kDa), NaCl (99%), NaF (99%), $YCl_3\cdot 6H_2O$ (99.99%), $YbCl_3\cdot 6H_2O$ (99.99%), $ErCl_3\cdot 6H_2O$ (99.9%), NH_4F (AR, 98%), and ethylene glycol (EG, 98%) were purchased from Beijing Chemical Co., Ltd. All materials were utilized without any further purification, and deionized water was utilized throughout the study.

2.2 Synthesis of CDs

Citric acid (CA, 1 g) and urea (2 g) were dissolved in 20 ml deionized water to form a transparent solution. Subsequently, the solution was transferred into an autoclave (50 ml) and placed in an oven for heating at 160 °C for 4 h. After cooling down to room temperature, the obtained suspensions were subjected to centrifugation at 10 000 rpm for 10 min to remove any unreacted small molecules. And then the resulting solution was underwent purification through silica-gel column chromatography employing a gradient elution comprising a 1 : 8 of mixture of methanol and methylene chloride. Finally, the purified solution was further concentrated by rotary evaporation, after which it was re-dissolved in deionized water for further measurements or usage. The concentration of CDs was determined by a calibrated thermogravimetric-analysis method, whereby the content of CDs was confirmed according to the position of the exothermic peak in Differential Thermal Analysis.

2.3 Synthesis of α-$NaYF_4$:18%Yb^{3+},2%Er^{3+} NPs

The synthesis of this compound was previously reported by Wang *et al.*[32] The general process involved the addition of NaCl (2.4 mmol), YCl_3 (0.96 mmol), $YbCl_3$ (0.216 mmol), $ErCl_3$ (0.024 mmol), and PEI (0.3 g) were added to a well-agitated transparent solution of EG (18 ml). Subsequently, a solution of NH_4F (4.8 mmol), dissolved in 12 ml of EG, was added to the aforementioned solution. The resulting mixture was stirred vigorously for 10 min at room temperature, then transferred to a 50 ml of autoclave, and subsequently heated at 200 °C for 2 h. The obtained NPs were collected by centrifugation, washed with ethanol and deionized water several times, and finally dried in an oven at 80 °C for 12 h.

2.4 Synthesis of β-$NaYF_4$:18%Yb^{3+},2%Er^{3+}@CDs composites

The as-prepared α-$NaYF_4$:18%Yb^{3+},2%Er^{3+} (100 mg) NPs and NaF (22 mg) were added in deionized water, which was mixed with a total volume of 8 ml solution containing CDs (mass ratio of α-$NaYF_4$:18%Yb^{3+},2%Er^{3+} : CDs = 1 : 1, 1 : 2, 1 : 4, 1 : 6, and 1 : 8, denoted as β-NYF@1CDs, β-NYF@2CDs, β-NYF@4CDs, β-NYF@6CDs, and β-NYF@8CDs, respectively). The resulting mixture was agitated for a further 20 min, then transferred to a 20 ml of autoclave, and subsequently heated at 160, 180, and 200 °C for 8 h, respectively. The final products were obtained by centrifugation and washed with anhydrous ethanol for twice, and then dried at 80 °C for 12 h.

2.5 Characterization

The phase purity of the solid-state samples was evaluated by employing a PanAnalytical X'Pert powder diffractometer, using Cu K_α radiation. The surface morphology of the β-$NaYF_4$:18%Yb^{3+},2%Er^{3+}@CDs composites was visualized using a field-emission scanning electron microscope (SEM, Zeiss Sigma 500) and a transmission electron microscope (TEM, JEM 2100F). FT-IR spectra were obtained using an Aicolex Nexus 470, whereby the sample was mixed with a tablet of KBr. The Raman spectra were acquired using a Horiba LabRAM HR Evolution Raman spectrometer with a 633 nm laser light source. A steady-state and dynamic analysis of the spectra was conducted on an Edinburgh Instruments FLS980 fluorescence spectrometer, which was equipped with a single 0.22 m excitation and emission monochromator. For recording UC emission spectra, we used a 980 nm laser diode as the excitation source and a Hamamatsu R928 PMT for the detection of visible emission. For temperature dependent emission measurement, the samples were subjected to heating within a Linkam THMS600 temperature-controlled stage.

3. Results and discussion

In general, temperature is a significant factor influencing the cubic-to-hexagonal phase transformation of $NaYF_4$.[33] Fig. 1a–c show the XRD patterns of the samples prepared at temperatures of 160, 180, and 200 °C, respectively. It is evident that at milder reaction temperatures (160 and 180 °C), the presence of the α-$NaYF_4$ cubic phase (JCPDS card no. 77-2042) in the composites is clearly observed (see in Fig. 1a and b). As the temperature increases to 200 °C, only the hexagonal structure of $NaYF_4$ (JCPDS card no. 16-0334) is observed in the composites. This evidence indicates that an elevated reaction temperatures accelerate the phase transformation process. This conclusion is further substantiated by the associated SEM study of the morphological transition. As the reaction proceeded, the phase transformation was accompanied by a typical morphological variation from spherical NPs to the final microtubes, which has already been extensively studied by Li *et al.*[34] The sample prepared at 160 °C (β-NYF@6CDs) comprises a substantial number of NPs and a limited quantity of hollow rods, with a length of approximately 10 μm and a diameter of ~1 μm (see Fig. 1d). In contrast, the composite produced at 200 °C (Fig. 1f) exhibits exclusively hollow rods. These observations, coupled with additional characteristics of the morphology, suggest that this study could provide insights into the dynamics of phase transformations and phase morphologies. It is established that the hexagonal phase is thermodynamically stable and exhibits greater order than the α-$NaYF_4$ cubic phase. Thus, it can be concluded that the most stable hexagonal phase can be obtained by applying of sufficient thermal energy, which can be achieved by utilizing a high reaction temperature or prolonging the reaction time. In this instance, the α-$NaYF_4$:18%Yb^{3+},2%Er^{3+} NPs subjected to hydrothermal processing at 200 °C over an 8-hour period demonstrated a tendency to adopt a hexagonal phase structure as a consequence of the lengthy processing time and the availability of sufficient energy to overcome the associated energy barrier. The anisotropic unit cell structure of the hexagonal phase causes β-$NaYF_4$:18%Yb^{3+},2%Er^{3+} to induce anisotropic growth along the crystal-reactive directions, resulting in the formation of hexagonal structures, specifically a hollow rod-like morphology (see Fig. 1e and f). It is noteworthy that no diffraction peak indicative of CDs was detected in any of the samples, which is likely due to the minimal quantity of CDs present in the composite. Moreover, as observed regarding the effect on the morphology, the combination with CDs exhibited a negligible effect on the phase transformation.

To gain insight into the impact of CDs on the composites, a comprehensive examination of the microstructural characteristics of the composites was conducted. Fig. 2a and b show representative TEM and high-resolution TEM images of the β-

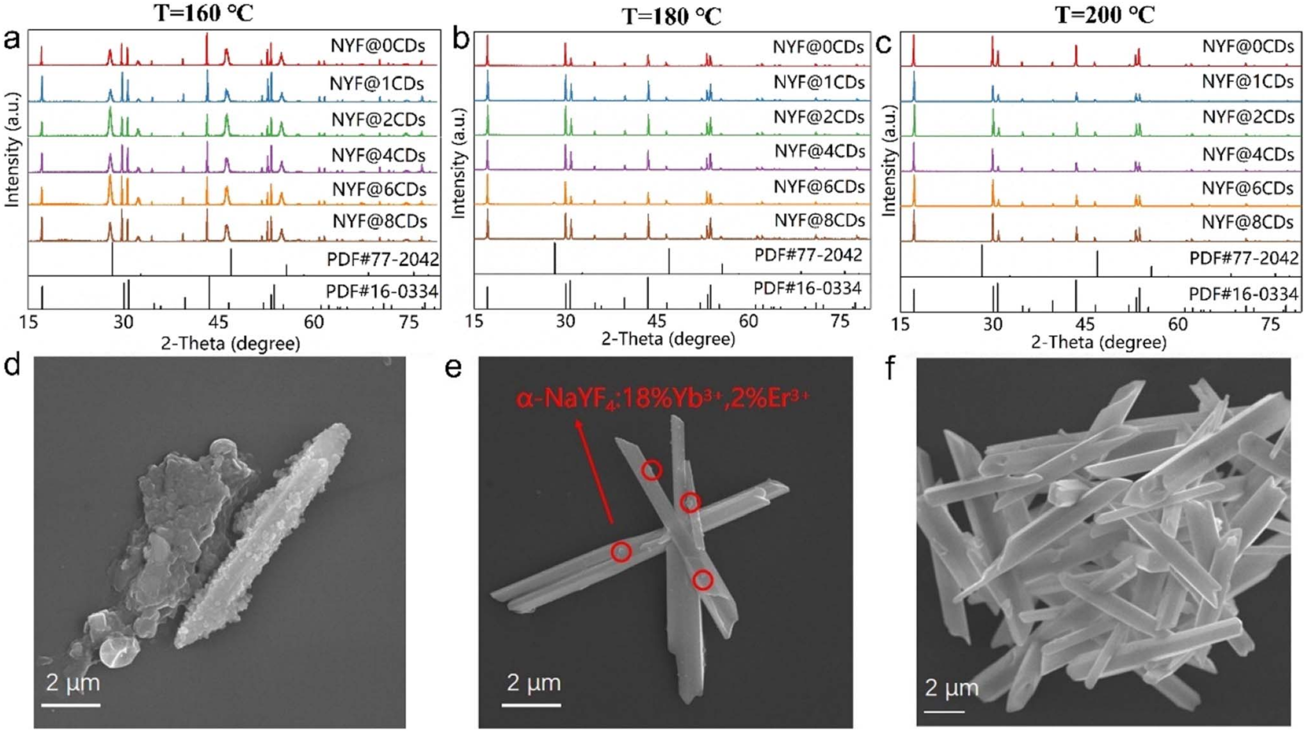

Fig. 1 XRD patterns of β-$NaYF_4$:18%Yb^{3+},2%Er^{3+}@CDs composites at various reaction temperature (a) 160, (b) 180, and (c) 200 °C; typical SEM images of the β-NYF@6CDs sample at various reaction temperature (d) 160 °C, (e) 180 °C, and (f) 200 °C.

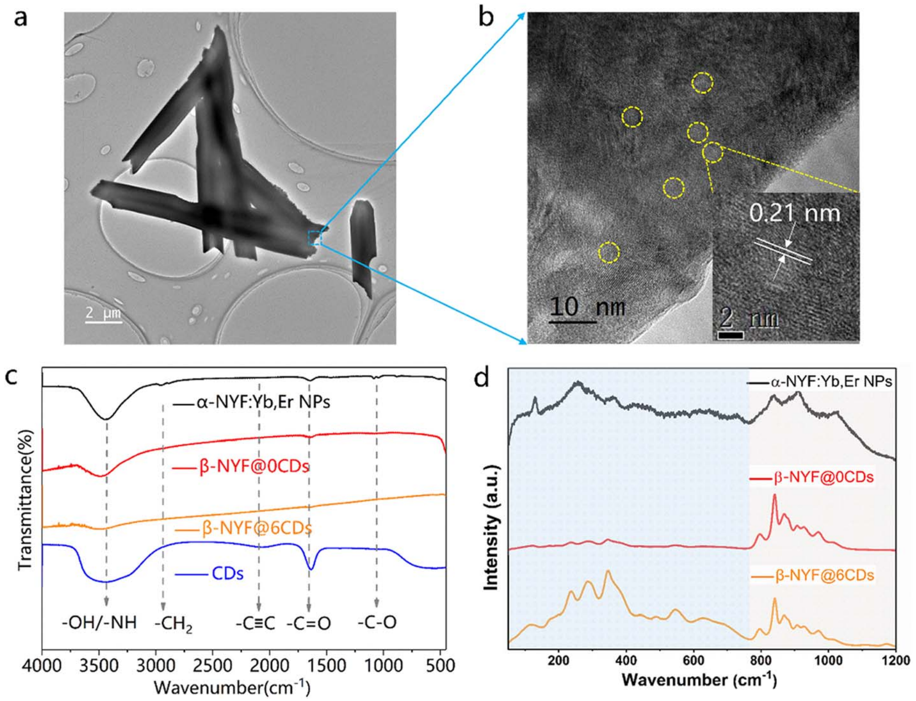

Fig. 2 (a) A typical TEM and (b) a high-resolution TEM image of the β-NYF@6CDs composite; (c) FT-IR spectra of α-$NaYF_4$:18%Yb^{3+},2%Er^{3+} NPs, β-$NaYF_4$:18%Yb^{3+},2%Er^{3+} sample, CDs powder, and the β-NYF@6CDs composite; (d) Raman spectra of α-$NaYF_4$:18%Yb^{3+},2%Er^{3+} NPs, β-$NaYF_4$:18%Yb^{3+},2%Er^{3+} sample, and the β-NYF@6CDs composite.

NYF@6CDs composite prepared at 200 °C for 8 h. In the high-magnification TEM image (Fig. 2b), in which CDs (yellow circles) are visible on the surface of the hollow rods, confirming the successful incorporation of CDs into the β-$NaYF_4$:18% Yb^{3+},2%Er^{3+} hollow rods. The interplanar distance between adjacent lattice fringes was estimated to be approximately 0.21 nm (as shown in the inset of Fig. 2b), which aligns with the *d*-spacing value of the (100) facet of graphitic carbon (Fig. S1†). This finding suggests that CDs are integrated into the evolving crystals of β-$NaYF_4$:18%Yb^{3+},2%Er^{3+} during the phase transformation, resulting in the formation of the β-$NaYF_4$:18% Yb^{3+},2%Er^{3+}@CDs composite. Further evidence is provided by the FT-IR and Raman spectra, as shown in Fig. 2c and d. Following the phase transformation from α-$NaYF_4$:18%Yb^{3+},2% Er^{3+} nanospheres to β-$NaYF_4$:18%Yb^{3+},2%Er^{3+} hollow rods, there is minimal change in the absorption peaks observed in the FT-IR spectra, with the exception of a weaker absorption band centered at approximately 3435 cm^{-1}, which is attributed to the stretching vibration of OH^- groups.

Notably, this absorption band is significantly diminished in the β-$NaYF_4$:18%Yb^{3+},2%Er^{3+}@CDs composite, indicating a reduction in OH^- groups following the incorporation of CDs within the β-$NaYF_4$:18%Yb^{3+},2%Er^{3+}@CDs hollow rods. This conclusion is supported by the Raman analysis, as depicted in Fig. 2d. The Raman spectra of α-$NaYF_4$:18%Yb^{3+},2%Er^{3+} and β-$NaYF_4$:18%Yb^{3+},2%Er^{3+}@CDs can be divided into two distinct regions. The peaks observed between 100 and 750 cm^{-1} are attributed to the vibrational features of the fluoride, while those in the range of 750 to 1200 cm^{-1} are believed to originate from the phonon frequencies of Y–OH, which is associated with the poor resistance of the host material against hydrolysis, a conclusion that is corroborated by the literature.[35] It is evident that the intensities of the high phonon vibrational bands are reduced in the β-NYF@6CDs sample compared to those observed in β-$NaYF_4$:18%Yb^{3+},2%Er^{3+}. This reduction may be attributed to a decrease in surface defects, specifically the OH^- moiety, facilitated by the diffusion of atoms during the incorporation of CDs. The results suggest that OH^- defects are present on the particle surfaces and that their concentration decreases following the introduction of CDs into the composites. In consideration of the structure of CDs, carboxyl terminals (–COO–) are abundant on the surface of CDs and are capable of attracting lanthanide ions through electrostatic interaction due to their negative charge. Consequently, the cubic-to-hexagonal phase transformation of $NaYF_4$ is expected to be accompanied by a reduction in the number of hydroxyl groups present within the crystal structure.

It is well-established that lanthanide ions incorporated into larger particles of hexagonal $NaYF_4$ (nano)crystal demonstrate a high UC efficiency.[33,36] To investigate the impact of CDs on the UC emission behavior of the as-prepared samples, we conducted measurements of the UC emission spectra for all samples under excitation by a 980 nm laser diode (LD) at room temperature (Fig. 3a–c). All samples exhibit two distinct emission bands associated with Er^{3+}, specifically the green ($^2H_{11/2}$,$^4S_{3/2}$ → $^4I_{15/2}$) and the red ($^4F_{9/2}$ → $^4I_{15/2}$) emissions. In comparison to α-$NaYF_4$:18%Yb^{3+},2%Er^{3+} NPs, the emission intensity shows a significant increase for the β-$NaYF_4$:18%

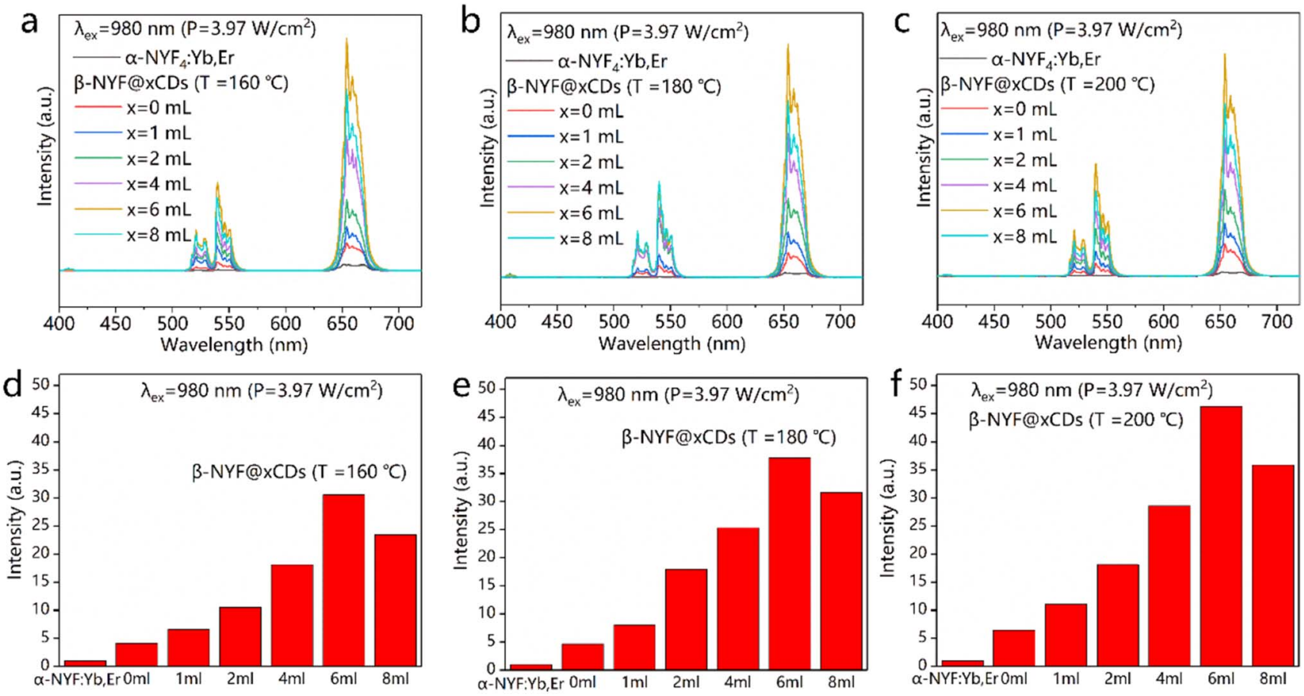

Fig. 3 UC emission spectra of β-$NaYF_4$:18%Yb^{3+},2%Er^{3+}@CDs composites at various reaction temperature: (a) 160, (b) 180, and (c) 200 °C; the total integrated emission intensity for the samples is presented as a function of the amount of CDs.

Yb^{3+},2%Er^{3+} micro hollow rods due to phase transformation, as anticipated (see Fig. 3a–c). Notably, the introduction of CDs has led to a substantial enhancement in the emission intensity of the composites, peaking at a mass ratio of $NaYF_4 : CDs = 1 : 6$, followed by a subsequent decline. For clarity, the integrated emission intensities (ranging from 505 to 570 nm for the green emission bands and from 625 to 700 nm for the red emission band) for all samples have been calculated and presented in Fig. 3d–f. It is evident that β-$NaYF_4$:18%Yb^{3+},2%Er^{3+}@CDs composites exhibit a markedly stronger emission intensity compared to α-$NaYF_4$:18%Yb^{3+},2%Er^{3+} NPs, with a 45-fold enhancement observed for the β-NYF@6CDs sample prepared at 200 °C. These results confirm that the CDs can enhance the efficiency of UC emission in β-$NaYF_4$:18%Yb^{3+},2%Er^{3+}@CDs composites.

To gain insight into the underlying mechanism of UC enhancement in composites, we investigate the dependence of UC emission intensity on excitation power (see Fig. S2†). For nearly all UC mechanism, the UC emission intensity (I_{UC}) is proportional to a specific power (n) of the near-infrared excitation intensity (I_{NIR}):

$$I_{UC} = I_{NIR}{}^{n} \tag{1}$$

where n represents the number of NIR photons absorbed per visible photon emitted, the slope of a log–log curve can be utilized to determine the power dependence of UC. Fig. 4a–c show the UC emission intensity as a function of excitation power on a double logarithmic scale for the red and green emissions in the as-prepared α-$NaYF_4$:18%Yb^{3+},2%Er^{3+} NPs, β-$NaYF_4$:18%Yb^{3+},2%Er^{3+}, and β-NYF@6CDs samples, respectively. The slope values for the red emission were determined to be 1.81, 1.91, and 2.14 for the α-$NaYF_4$:18%Yb^{3+},2% Er^{3+} NPs, β-$NaYF_4$:18%Yb^{3+},2%Er^{3+}, and β-NYF@6CDs samples, respectively. In contrast, the slope values for the green emission were found to be 1.64, 1.61, and 1.85, respectively. This observation thus suggests that both the green and red emissions are associated with a two-photon absorption process. The log–log slope values exhibit a similar trend, suggesting that the underlying UC mechanism remains unchanged with the introduction of CDs. This finding aligns with the typical scenario of the UC emission mechanism involving the Yb^{3+}/Er^{3+} couple, which has been well-documented in the literature.[37] A simplified energy scheme is shown in Fig. 4d. Briefly, the red and green UC emissions are both the result of a two-step energy transfer from the Yb^{3+} to the Er^{3+}. Initially, under 980 nm excitation, the Yb^{3+} ion functions as a sensitizer, thereby transferring the energy to populate electrons in the Er^{3+}:$^4I_{11/2}$ state. In the event of the energy transfer occurring once more prior to the decay of the excited Er^{3+} ion back to the ground sate, the Er^{3+} ion is excited to the $^4F_{7/2}$ level. This results in a non-radiative decay to the $^2H_{11/2}$ and $^4S_{3/2}$ levels, from which the green emission is produced. A subset of Er^{3+} ions in the $^4S_{3/2}$ state undergo non-radiative decay into the closely related $^4F_{9/2}$ level, thus giving rise to the red luminescence. It is important to note that the deviation from the expected slope of 2 is a commonly observed phenomenon. This deviation can be attributed to the competition among various decay channels within the intermediate state, including multi-phonon relaxation to the lower-lying states, radiative decay to the ground state, UC from the intermediate state, and non-radiative trapping.[38] In the low-power regime, inefficient non-radiative

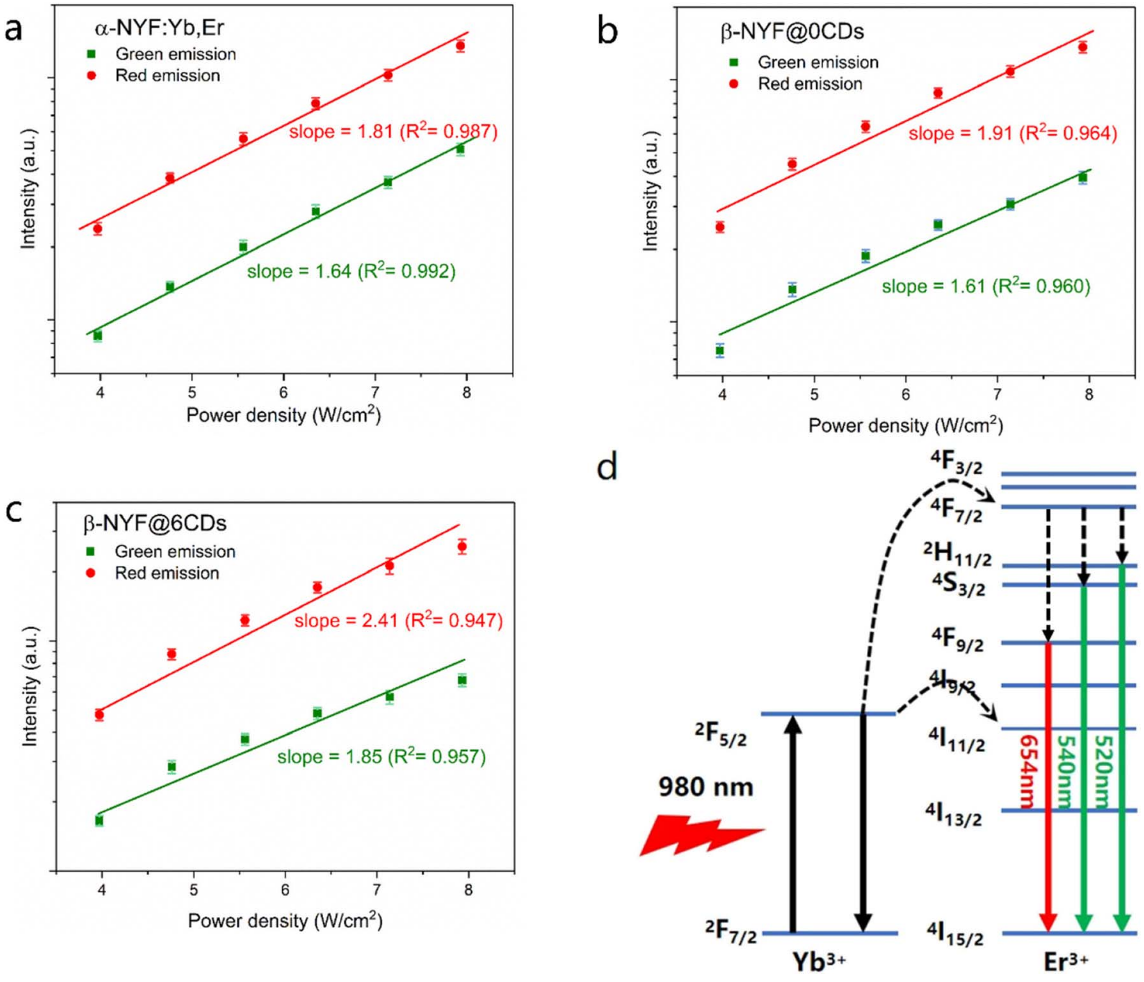

Fig. 4 Emission intensity as a function of excitation pump power for (a) as-prepared α-$NaYF_4$:18%Yb^{3+},2%Er^{3+} NPs, (b) β-$NaYF_4$:18%Yb^{3+},2%Er^{3+}, and (c) β-NYF@6CDs samples; (d) schematic representation of the UC mechanism in the Yb^{3+} and Er^{3+} codoped system.

channels tend to favor the UC process. This is exemplified by the higher value of n observed in the present case. It is evident that the slope values (n) increase gradually from α-$NaYF_4$:18%Yb^{3+},2%Er^{3+}, to β-$NaYF_4$:18%Yb^{3+},2%Er^{3+}, and finally to β-NYF@6CDs composite. This finding aligns well with the observed enhancement of UC emission, as illustrated in Fig. 3.

Fig. 5a shows the luminescence decay curves of CDs for the β-NYF@6CDs sample with various reaction temperatures. It is evident that all decay curves display non-exponential decay characteristics, which can be modeled using a double exponential function:

$$I(t) = A_1 \exp\left(\frac{t}{\tau_1}\right) + A_2 \exp\left(\frac{t}{\tau_2}\right) \quad (2)$$

where $I(t)$ represents the intensity at a given time t, A_1 and A_2 are constants, τ is the time interval, and τ_1 and τ_2 denote the short- and long-decay components, respectively. The average decay times ($\tau_{\rm avr}$) are defined as follows:

$$\tau_{\rm avr} = \frac{A_1{\tau_1}^2 + A_2{\tau_2}^2}{A_1\tau_1 + A_2\tau_2} \quad (3)$$

based on the equations presents in eqn (2) and (3), the average lifetime can be calculated and is observed to decrease steadily with increasing reaction temperature, from $\tau = 3.69$ ns (for $T = 160$ °C) to $\tau = 3.09$ ns (for $T = 200$ °C). This phenomenon can be attributed to the fact that elevated hydrothermal temperatures lead to a transformation of the surface of CDs, thereby accelerating the rate of non-radiative relaxation of excitons.[39,40] This also indicates that a higher reaction temperature may facilitate the combination of α-$NaYF_4$:18%Yb^{3+},2%Er^{3+} NPs and CDs, but it may also result in a deterioration of the emission intensity of the CDs, which could be disadvantageous for constructing a composite with dual-mode luminescence properties. Notably, the incorporation of CDs into the composite leads to a substantial enhancement of UC emission. Further insight into the underlying mechanism of UC enhancement can be gained by examining the decay dynamics of UC emission. Fig. 5b and c show the UC luminescence decay curves for the $^4S_{3/2} \rightarrow {}^4I_{15/2}$ (540 nm) and $^4F_{9/2} \rightarrow {}^4I_{15/2}$ (654 nm) transitions of the prepared samples, respectively. The average lifetimes for the various emission bands can be determined by employing eqn (2) and (3) to fit the decay curves. It is evident that the prolonged lifetimes

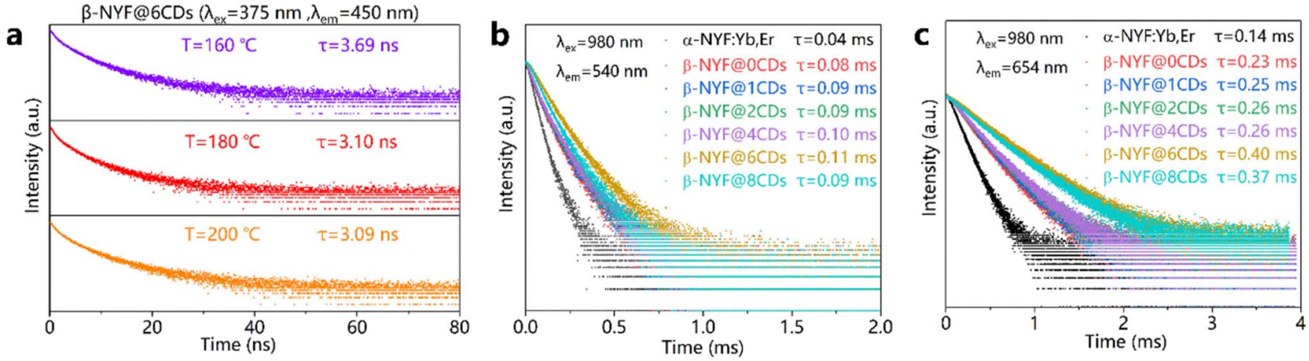

Fig. 5 (a) Luminescence decay curves of the β-NYF@6CDs composite at different reaction temperatures; luminescence decay curves of (b) green and (c) red emissions for β-$NaYF_4$:18%Yb^{3+},2%Er^{3+}@CDs composites with varying content of CDs.

observed for the two UC emissions are accompanied by a change in crystal phase, transitioning from cubic to hexagonal. This result supports the correlation between luminescence decay kinetics and the lattice phase. With the introduction of increasing amounts of CDs into the hexagonal phase, the average lifetimes of both UC emissions initially increase and then decrease with higher concentrations. This trend in the decay lifetime is consistent with the results of the steady-state measurements, as presented in Fig. 3.

The aforementioned results substantiate the enhancement of UC emissions and the extension of the decay lifetime of excited energy levels through the formation of a composite between α-$NaYF_4$:18%Yb^{3+},2%Er^{3+} NPs and CDs. In view of the influence of CDs on the microstructural characteristics of composites, it seems reasonable to posit that the incorporation of CDs into these materials may enhance UC emission, potentially due to the elimination of surface hydroxyl groups that are inherent to composites produced *via* hydrothermal synthesis. In general, during the synthesis of α-$NaYF_4$:18%Yb^{3+},2%Er^{3+} NPs, OH^- ions are likely to substitute some native F^- sites on the nanoparticle surface, which can act as highly efficient luminescence quenchers.[41] This phenomenon is the primary factor contributing to the reduced UC efficiency observed in NPs compared to their bulk counterparts. The higher excited states of lanthanide ions are effectively quenched due to coupling with the vibrations of hydroxyl ions incorporated into the crystal structure. The pyrolysis of CDs into small fragments, caused by the applied heating treatment, is evidenced by the observed reduction in the lifetime of the CDs, as shown in Fig. 5a. The resulting small fragments remain attached to the surface of the α-$NaYF_4$:18%Yb^{3+},2%Er^{3+} NPs and bond with the lanthanide ions to form the composites. It is possible that the CD fragments may influence the nucleation and growth of the α-$NaYF_4$:18%Yb^{3+},2%Er^{3+} NPs, potentially preventing the incorporation of OH^- into the $NaYF_4$ lattice and thus suppressing the surface-dopant-induced quenching of excitation energy. In the $NaYF_4$ UC NPs co-doped with Yb^{3+} and Er^{3+}, the near-infrared levels $^4I_{11/2}$ (Er^{3+}) and $^2F_{5/2}$ (Yb^{3+}) have been observed to be quenched. The quenching process has been shown to be due to coupling to the OH-vibration of hydroxyl ions incorporated in the crystal structure, and by energy migration to the surface, which was found to be the strongest contribution to reduced UC emission.[42] Therefore, it can be concluded that the reduction of OH^- groups *via* CDs and the blockage of the non-radiative transition channels in this study are the primary factors responsible for the observed enhancement of UC emission and the prolongation of the Er^{3+} lifetime. In addition to the reduction in surface defects observed in the NPs, the incorporation of excess CDs into the NPs can also induce a greater degree of local lattice distortion, ultimately leading to a decrease in UC emission intensity. These findings provide a potential explanation for the observed enhancement in UC emission intensity and decay lifetime of β-$NaYF_4$:18%Yb^{3+},2%Er^{3+}@CDs composites, which aligns with previously reported results.

Optical temperature sensing has emerged as a significant area of research within the Er^{3+}-doped system, primarily due to the narrow energy gap between the $^2H_{11/2}$ and $^4S_{3/2}$ levels of Er^{3+}.[43] It is well established that the two green emission levels will remain in a thermal equilibrium at all temperatures due to their thermally coupled nature. The populations of the $^2H_{11/2}$ and $^4S_{3/2}$ levels conform to the Boltzmann distribution law. The relationship between the fluorescence intensity ratio (FIR) of these two green emissions and temperature can be expressed as follows:

$$\mathrm{FIR} = \frac{I_S}{I_H} = A\exp\left(\frac{\Delta E}{kT}\right) \tag{4}$$

where I_S and I_H denote the integrated intensities of the radiative relaxations from the $^4S_{3/2}$ and $^2H_{11/2}$ excited states to the $^4I_{15/2}$ ground state, respectively. The parameter A is a constant that is independent of the sample temperature but does depend on the spontaneous emission rate, level of degeneracy, and photon energy. The symbol ΔE represents the energy gap between the $^2H_{11/2}$ and $^4S_{3/2}$ levels, k is the Boltzmann constant, and T is the absolute temperature.

To investigate the composites as temperature probes, we recorded the emission spectra of the samples at varying temperatures. Fig. 6a shows the UC emission spectra of the β-NYF@6CDs composite, recorded at temperatures ranging from 298 K and 473 K, with intervals of 25 K. Upon excitation at 980 nm, the characteristic luminescence peaks corresponding to the $^2H_{11/2} \rightarrow {}^4I_{15/2}$ and the $^4S_{3/2} \rightarrow {}^4I_{15/2}$ transitions are observable at all temperatures. The spectra have been normalized to the maximum intensity of the $^4S_{3/2}$–$^4I_{15/2}$ emission peak. As anticipated for thermally coupled excited states, the intensity ratio between these peaks changes a change with increasing temperature. The spectral regions depicted by I_H and I_S are determined by the integrated emission intensity in the range of 505–535 nm and 535–570 nm, respectively, in the same temperature range. The dependence of FIR on the absolute temperature is shown in Fig. 6b. The experimental data were fitted using eqn (4), and the fitted results are shown in Fig. 6b by a solid black line. As a result of the fitting process, the value of the pre-exponential constant (A) value was determined to be 0.12. Furthermore, the energy difference between the excited states (ΔE) was found to be 666 cm^{-1} in the composite, which closely aligns with the values reported in the literature.[44,45] It is plausible that the observed discrepancies arise from the presence of two overlapping emission bands: $^2H_{11/2} \rightarrow {}^4I_{15/2}$ and $^4S_{3/2} \rightarrow {}^4I_{15/2}$. Additionally, the report indicates that non-radiative cross-relaxation processes also influence the observed FIR values. Based on the fitted energy gap, the performance of this thermometer is expressed in terms of both the absolute and relative sensitivities (S_a and S_r), which can be defined as follows:

$$S_a = \left|\frac{\mathrm{d(FIR)}}{\mathrm{d}T}\right| = A \times \frac{\Delta E}{kT^2}\exp\left(\frac{\Delta E}{kT}\right) \tag{5}$$

$$S_r = \left|\frac{1}{\mathrm{(FIR)}}\frac{\mathrm{d(FIR)}}{\mathrm{d}T}\right| = \frac{\Delta E}{kT^2} \tag{6}$$

By inserting the values derived above into eqn (5) and (6), it is possible to obtain the S_a and S_r as functions of temperature from 298 to 473 K for the composite, as illustrated in Fig. 6c and d. The results indicate that both the S_a and S_r decrease with increasing temperature, reaching maximum values of 0.0032 K^{-1} and 1.08% K^{-1}, respectively, at 298 K (see eqn (S1)–(S3)†). Similarly, the temperature-sensing performance of α-NaYF$_4$:18%Yb^{3+},2%Er^{3+} NPs have also been subjected to a systematically investigated as a luminescence thermometer, with the findings presented in Fig. S3 and eqn (S4)–(S6).† The S_r value is independent of the operational principle of the thermometer, allowing for a direct and quantitative comparison of various thermometers.[46,47] It is evident that the sensitivity of the composite is greater than that of the α-NaYF$_4$:18%Yb^{3+},2%Er^{3+} NPs across the entire measured temperature range, indicating

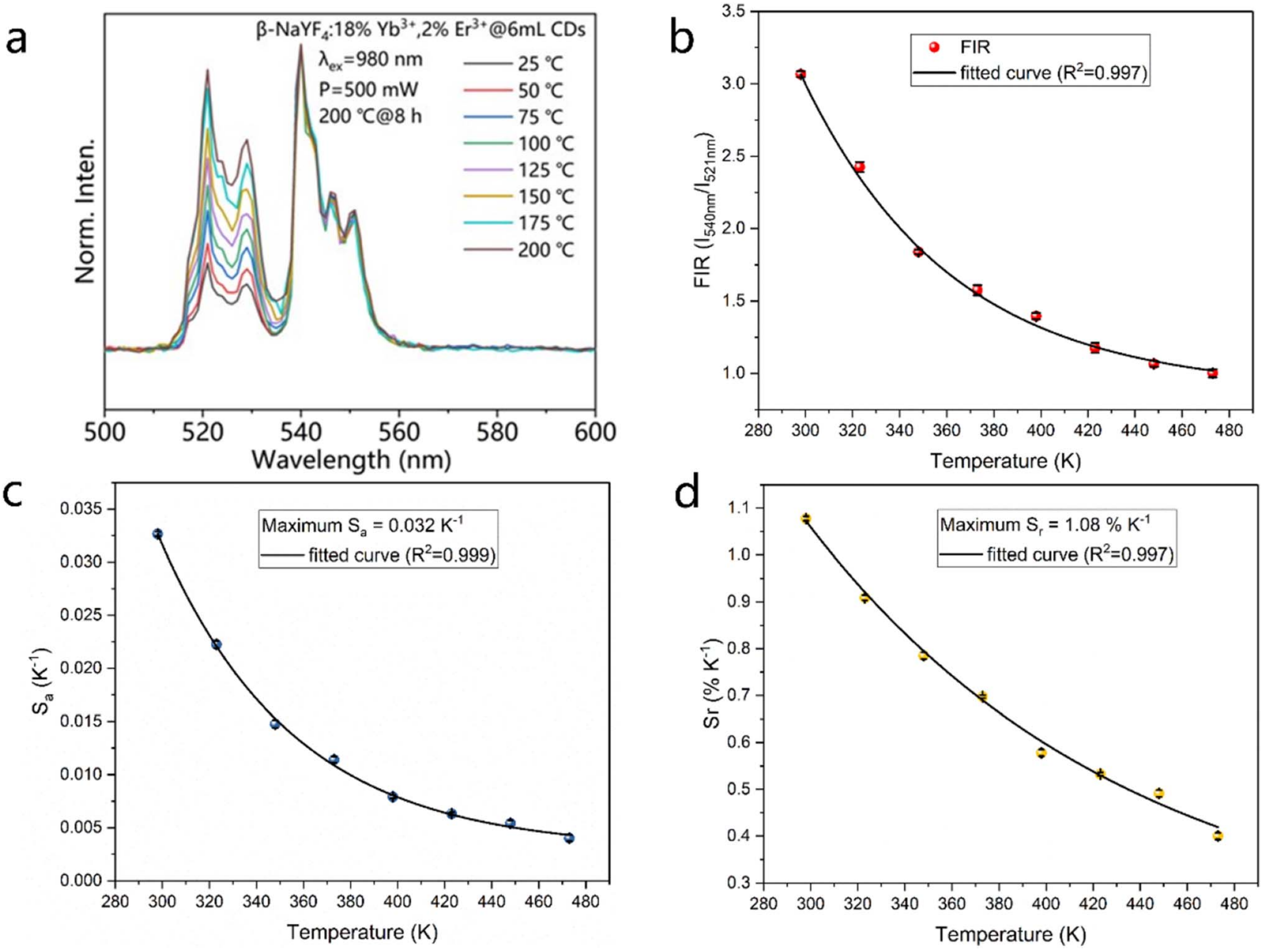

Fig. 6 (a) The normalized UC emission spectra as a function of temperature for the β-NYF@6CDs composite; (b–d) the parameters of FIR, S_a, and S_r as functions of temperature.

Table 1 Thermographic properties of some Yb^{3+}/Er^{3+}-codoped systems as luminescence probes

Material	Range (K)	Max. S_r (% K^{-1})	T_{max} (K)	Ref.
YVO_4:Yb/Er	315–483	0.78	380	48
$CaWO_4$:Yb,Er	300–540	1.01	480	49
$LuVO_4$:Yb,Er@SiO_2	303–353	0.82	303	50
Ca_2MgWO_4:Yb,Er	303–573	0.92	303	51
β-$NaYF_4$:Yb,Er@CDs	298–473	1.08	298	This work

that the composite exhibits superior temperature-sensing performance. These results were comparable to the reported results in Yb^{3+}/Er^{3+} codoped systems listed in Table 1. Moreover, Fig. S4† presents the values of temperature uncertainty (δT) as determined by eqn (S1)† with respect to temperature ranging from 298 K to 473 K. It is evident that the minimum values of δT are 0.38 K and 0.49 at 298 K for the β-NYF@6CDs composite and α-$NaYF_4$:18%Yb^{3+},2%Er^{3+} NPs, respectively. It is noteworthy that the composite demonstrates significantly enhanced UC emission at the same excitation density, which is advantageous in practical applications.

4. Conclusions

In summary, the synthesis of β-$NaYF_4$:18%Yb^{3+},2%Er^{3+}@CDs composites was successfully achieved by combining α-$NaYF_4$:18%Yb^{3+},2%Er^{3+} NPs with CDs through the cubic-to-hexagonal phase transformation of $NaYF_4$. The successful formation of the composites was confirmed through morphological and structural characterization. The experimental results demonstrated that the incorporation of CDs led to a reduction in the number of OH^- groups, which act as quenching centers in the composites. This reduction prolongs the luminescence lifetime of the excited energy levels of Er^{3+} ions and enhances the UC emission. This study paves the way for advancements in the UC emission of lanthanide ions and the modulation of the luminescence lifetime through the construction of composites. Moreover, the optical temperature-sensing characteristics of thermally coupled green levels were identified and evaluated. The maximum S_a and S_r were found to be 0.0032 K^{-1} and 1.08% K^{-1} at 298 K, respectively, indicating their potential application in optical temperature sensors and fluorescence detection.

Data availability

The authors confirm that the data supporting the findings of this study are available within the article and/or its ESI.†

Conflicts of interest

There are no conflicts to declare.

Acknowledgements

Financial supports from the National Natural Science Foundation of China (Grant No. 52002289) and Science Foundation for High-Level Talents of Wuyi University (Grant No. 2019AL034) are gratefully acknowledged. This work is also supported by the Natural Science Foundation of Guangdong province (No. 2022A1515011669), Major Science and Technology Research and Development Project of Jiangxi Province (20223AAE01003) and Science Foundation for Young Teachers of Wuyi University (No. 2019td03).

References

1 H. Dong, L. D. Sun and C. H. Yan, Local structure engineering in lanthanide-doped nanocrystals for tunable upconversion emissions, *J. Am. Chem. Soc.*, 2021, **143**, 20546–20561, DOI: 10.1021/jacs.1c10425.

2 Y. Zhang, X. Zhu and Y. Zhang, Exploring heterostructured upconversion nanoparticles: from rational engineering to diverse applications, *ACS Nano*, 2021, **15**, 3709–3735, DOI: 10.1021/acsnano.0c09231.

3 K. Du, J. Feng, X. Gao and H. Zhang, Nanocomposites based on lanthanide-doped upconversion nanoparticles: diverse designs and applications, *Light: Sci. Appl.*, 2022, **11**, 222.

4 D. Yuan, M. C. Tan, R. E. Riman and G. M. Chow, Comprehensive study on the size effects of the optical properties of $NaYF_4$:Yb,Er nanocrystals, *J. Phys. Chem. C*, 2013, **117**, 13297–13304, DOI: 10.1021/jp403061h.

5 Q. Li, X. Xie, H. Wu, H. Chen, W. Wang, X. Kong and Y. Chang, Superenhancement photon upconversion nanoparticles for photoactivated nanocryometer, *Nano Lett.*, 2023, **23**, 3444–3450.

6 X. Wu, Y. Chen, R. Li, Q. Zeng and T. Yu, Construction of interfacial energy transfer nanoplatforms using carbon dots and $NaYF_4$:Eu^{3+} nanoparticles, *Ceram. Int.*, 2024, **50**, 31014–31022, DOI: 10.1016/j.ceramint.2024.05.406.

7 L. Wang, X. Li, Z. Li, W. Chu, R. Li, K. Lin, H. Qian, Y. Wang, C. Wu, J. Li, D. Tu, Q. Zhang, L. Song, J. Jiang, X. Chen, Y. Luo, Y. Xie and Y. Xiong, A new cubic phase for a $NaYF_4$ host matrix offering high upconversion luminescence efficiency, *Adv. Mater.*, 2015, **27**, 5528–5533, DOI: 10.1002/adma.201502748.

8 D. Yu, T. Yu, H. Lin, S. Zhuang and D. Zhang, Recent advances in luminescent downconversion: new materials, techniques, and applications in solar cells, *Adv. Opt. Mater.*, 2022, **10**, 2200014, DOI: 10.1002/adom.202200014.

9 L. Ruiyi, L. Zaijun, S. Xiulan, J. Jan, L. Lin, G. Zhiguo and W. Guangli, Graphene quantum dot-rare earth upconversion nanocages with extremely high efficiency of upconversion luminescence, stability and drug loading towards controlled delivery and cancer theranostics, *Chem. Eng. J.*, 2020, **382**, 122992, DOI: 10.1016/j.cej.2019.122992.

10 M. Zou, Y. Zhao, B. Ding, F. Jiang, Y. Chen, P. Ma and J. Lin, NIR-triggered biodegradable MOF-coated upconversion nanoparticles for synergetic chemodynamic/photodynamic therapy with enhanced efficacy, *Inorg. Chem. Front.*, 2021, **8**, 2624–2633, DOI: 10.1039/D1QI00252J.

11 H. Yang, Y. Liu, Z. Guo, B. Lei, J. Zhuang, X. Zhang, Z. Liu and C. Hu, Hydrophobic carbon dots with blue dispersed

emission and red aggregation-induced emission, *Nat. Commun.*, 2019, **10**, 1789, DOI: **10.1038/s41467-019-09830-6**.

12 L. Đorđević, F. Arcudi, M. Cacioppo and M. Prato, A multifunctional chemical toolbox to engineer carbon dots for biomedical and energy applications, *Nat. Nanotechnol.*, 2022, **17**, 112–130.

13 B. Wang and S. Lu, The light of carbon dots: From mechanism to applications, *Matter*, 2022, **5**, 110–149.

14 H. Wang, L. Ai, H. Song, Z. Song, X. Yong, S. Qu and S. Lu, Innovations in the solid-state fluorescence of carbon dots: strategies, optical manipulations, and applications, *Adv. Funct. Mater.*, 2023, **33**, 2303756.

15 Y. Chen, H. Lian, Y. Wei, X. He, Y. Chen, B. Wang, Q. Zeng and J. Lin, Concentration-induced multi-colored emissions in carbon dots: origination from triple fluorescent centers, *Nanoscale*, 2018, **10**, 6734–6743.

16 Y. Liu, B. Wang, Y. Zhang, J. Guo, X. Wu, D. Ouyang, S. Chen, Y. Chen, S. Wang and G. Xing, Perylenedioic acid-derived carbon dots with near 100% quantum yield in aqueous solution for lasing and lighting, *Adv. Funct. Mater.*, 2024, **34**, 2401353.

17 D. Li, E. V. Ushakova, A. L. Rogach and S. Qu, Optical properties of carbon dots in the deep-red to near-infrared region are attractive for biomedical applications, *Small*, 2021, **17**, 2102325.

18 J. Huang, Y. Chen, P. Rao, Z. Ni, X. Chen, J. Zhu, C. Li, G. Xiong, P. Liang and X. He, Enhancing the electron transport, quantum yield, and catalytic performance of carbonized polymer dots via Mn-O bridges, *Small*, 2022, **18**, 2106863.

19 R. Li, X. Wu, Y. Chen, Q. Zeng, T. Deng and T. Yu, Developing luminescent ratiometric thermometers based on dual-emission of $NaMgF_3$:Eu^{3+}/carbon dot nanocomposites, *ACS Appl. Nano Mater.*, 2024, **7**, 15288–15297, DOI: **10.1021/acsanm.4c02103**.

20 Y. Zhu, Z. Quan, B. Zhang, J. Zheng, J. Wang, X. Zhang, C. Zhang, T. Yang, X. He and S. Qu, Enhanced performance of carbon dots and Mn_3O_4 composite by phosphate in peroxymonosulfate activation, *Appl. Catal., B*, 2024, **351**, 123954.

21 Y. Chen, J. Zhu, H. Sheng, T. Yu and Q. Zeng, Superior thermal cycling stability of a carbon dots@$NaBiF_4$ nanocomposite: facile synthesis and surface configurations, *Dalton Trans.*, 2022, **51**, 8680–8687, DOI: **10.1039/d2dt00823h**.

22 Y. Zhao, B. He, E. Liu, J. Li, L. Wang, S. Chen, Y. Chen, Z. Tan, K. W. Ng and S. Wang, Aluminum-based surface polymerization on carbon dots with aggregation-enhanced luminescence, *J. Phys. Chem. Lett.*, 2021, **12**, 4530–4536.

23 M. Laurenti, M. Paez-Perez, M. Algarra, P. Alonso-Cristobal, E. Lopez-Cabarcos, D. Mendez-Gonzalez and J. Rubio-Retama, Enhancement of the upconversion emission by visible-to-near-infrared fluorescent graphene quantum dots for miRNA detection, *ACS Appl. Mater. Interfaces*, 2016, **8**, 12644–12651, DOI: **10.1021/acsami.6b02361**.

24 L. Ling, L. Ruiyi, W. Guangli, G. Zhiguo and L. Zaijun, Graphene quantum dots-$NaYF_4$:Yb,Er hybrid with significant enhancement of upconversion emission for fluorescent detection of carcinoembryonic antigen with exonuclease III-aided target recycling amplification, *Sens. Actuators, B*, 2019, **285**, 453–461, DOI: **10.1016/j.snb.2019.01.082**.

25 A. Zhou, F. Song, W. Yao, Y. Han, F. Song, W. Wu, C. Ming, D. Ju and A. Khan, Efficient solid-state and dual-mode photoluminescence of carbon-dots/$NaLuF_4$ microcrystals for multifunctional applications, *J. Alloys Compd.*, 2019, **775**, 457–465, DOI: **10.1016/j.jallcom.2018.10.125**.

26 N. Wang, Y. Yang, M. Zhang, Q. Zhu and Z. Li, Lysosomal adenosine triphosphate-activated upconversion nanoparticle/carbon dot composite for ratiometric imaging of hepatotoxicity, *Anal. Chem.*, 2022, **94**, 15738–15745, DOI: **10.1021/acs.analchem.2c03351**.

27 Y.-L. Sun, X.-P. Zhang, C.-X. Zhao, X. Liu, Y. Shu, J.-H. Wang and N. Liu, Upconversion nanoparticles/carbon dots (UCNPs@CDs) composite for simultaneous detection and speciation of divalent and trivalent iron ions, *Anal. Chim. Acta*, 2021, **1183**, 338973, DOI: **10.1016/j.aca.2021.338973**.

28 M. Li, W. Yao, J. Liu, Q. Tian, L. Liu, J. Ding, Q. Xue, Q. Lu and W. Wu, Facile synthesis and screen printing of dual-mode luminescent $NaYF_4$:Er,Yb (Tm)/carbon dots for anti-counterfeiting applications, *J. Mater. Chem. C*, 2017, **5**, 6512–6520, DOI: **10.1039/c7tc01585b**.

29 X. Xu, W. Li, W. Zhou, G. Tan, Y. Zheng, C. Hu, B. Lei, X. Zhang, Y. Liu and J. Zhuang, Preparation and properties of dual-mode luminescent $NaYF_4$:Yb,Tm@SiO_2/carbon dot nanocomposites, *J. Mater. Chem. C*, 2018, **6**, 10360–10366, DOI: **10.1039/c8tc03508c**.

30 Y. Zheng, H. Wei, P. Liang, X. Xu, X. Zhang, H. Li, C. Zhang, C. Hu, X. Zhang, B. Lei, W. Y. Wong, Y. Liu and J. Zhuang, Near-infrared-excited multicolor afterglow in carbon dots-based room-temperature afterglow materials, *Angew. Chem., Int. Ed.*, 2021, **60**, 22253–22259, DOI: **10.1002/anie.202108696**.

31 P. Liang, Y. Zheng, F. Liu, H. Shao, C. Hu, B. Lei, X. Zhang, Y. Liu, J. Zhuang and X. Zhang, General synthesis of carbon dot-based composites with triple-mode luminescence properties and high stability, *JACS Au*, 2023, **3**, 2291–2298.

32 F. Wang and X. Liu, Upconversion multicolor fine-tuning: visible to near-infrared emission from lanthanide-doped $NaYF_4$ nanoparticles, *J. Am. Chem. Soc.*, 2008, **130**, 5642–5643.

33 D. T. Klier and M. U. Kumke, Analysing the effect of the crystal structure on upconversion luminescence in Yb^{3+},Er^{3+}-co-doped $NaYF_4$ nanomaterials, *J. Mater. Chem. C*, 2015, **3**, 11228–11238, DOI: **10.1039/c5tc02218e**.

34 C. Li, Z. Quan, P. Yang, J. Yang, H. Lian and J. Lin, Shape controllable synthesis and upconversion properties of $NaYbF_4$/$NaYbF_4$:Er^{3+} and YbF_3/YbF_3:Er^{3+} microstructures, *J. Mater. Chem.*, 2008, **18**, 1353–1361, DOI: **10.1039/b717363f**.

35 M. M. Lage, R. L. Moreira, F. M. Matinaga and J.-Y. Gesland, Raman and infrared reflectivity determination of phonon modes and crystal structure of Czochralski-grown $NaLnF_4$ (Ln= La, Ce, Pr, Sm, Eu, and Gd) single crystals, *Chem. Mater.*, 2005, **17**, 4523–4529.

36 D. Yu, T. Yu, A. J. van Bunningen, Q. Zhang, A. Meijerink and F. T. Rabouw, Understanding and tuning blue-to-near-infrared photon cutting by the Tm^{3+}/Yb^{3+} couple, *Light: Sci. Appl.*, 2020, **9**, 107, DOI: **10.1038/s41377-020-00346-z**.

37 T. Xiao, Y. Li, T. Wang, Y. Fan, F. He, Q. Wang, J. Han, Z. Yin, Z. Yang, J. Qiu and Z. Song, Enhanced upconversion luminescence of $BiOCl:Yb^{3+},Er^{3+}$ nanosheets via carbon dot modification and their optical temperature sensing, *Mater. Chem. Front.*, 2021, **5**, 4280–4290, DOI: **10.1039/d0qm00589d**.

38 J. Suyver, A. Aebischer, S. García-Revilla, P. Gerner and H. U. Güdel, Anomalous power dependence of sensitized upconversion luminescence, *Phys. Rev. B: Condens. Matter Mater. Phys.*, 2005, **71**, 125123.

39 Y. Song, S. Zhu, S. Zhang, Y. Fu, L. Wang, X. Zhao and B. Yang, Investigation from chemical structure to photoluminescent mechanism: a type of carbon dots from the pyrolysis of citric acid and an amine, *J. Mater. Chem. C*, 2015, **3**, 5976–5984, DOI: **10.1039/c5tc00813a**.

40 J. Schneider, C. J. Reckmeier, Y. Xiong, M. von Seckendorff, A. S. Susha, P. Kasák and A. L. Rogach, Molecular fluorescence in citric acid-based carbon dots, *J. Phys. Chem. C*, 2017, **121**, 2014–2022, DOI: **10.1021/acs.jpcc.6b12519**.

41 Y. Wang, W. Lu, D. Yue, M. Wang, B. Tian, Q. Li, B. Hu, Z. Wang and Y. Zhang, A strategy to enhance the up-conversion luminescence of nanospherical, rod-like and tube-like $NaYF_4$: Yb^{3+}, Er^{3+} (Tm^{3+}) by combining with carbon dots, *CrystEngComm*, 2021, **23**, 935–943, DOI: **10.1039/d0ce01516d**.

42 F. T. Rabouw, P. T. Prins, P. V. Delgado, M. Castelijns, R. G. Geitenbeek and A. Meijerink, Quenching pathways in $NaYF_4:Er^{3+},Yb^{3+}$ upconversion nanocrystals, *ACS Nano*, 2018, **12**, 4812–4823, DOI: **10.1021/acsnano.8b01545**.

43 D. Li, W. Xu, Z. Huang, X. Jin, B. Xu, Z. Zhang, T. Zhang, D. Wang, X. Liu, H. Suo and Q. Li, Simultaneous enhancement of emission and thermal sensitivity via phase transition in $Gd_2(MoO_4)_3:Yb^{3+}/Er^{3+}$ crystals, *J. Am. Ceram. Soc.*, 2023, **106**, 438, DOI: **10.1111/jace.18756**.

44 S. Liu, H. Ming, J. Cui, S. Liu, W. You, X. Ye, Y. Yang, H. Nie and R. Wang, Color-tunable upconversion luminescence and multiple temperature sensing and optical heating properties of $Ba_3Y_4O_9:Er^{3+}/Yb^{3+}$ phosphors, *J. Phys. Chem. C*, 2018, **122**, 16289, DOI: **10.1021/acs.jpcc.8b04180**.

45 A. M. Kaczmarek, M. Suta, H. Rijckaert, T. P. van Swieten, I. Van Driessche, M. K. Kaczmarek and A. Meijerink, High temperature (nano)thermometers based on $LiLuF_4:Er^{3+},Yb^{3+}$ nano- and microcrystals. Confounded results for core–shell nanocrystals, *J. Mater. Chem. C*, 2021, **9**, 3589, DOI: **10.1039/d0tc05865c**.

46 D. Yu, H. Li, D. Zhang, Q. Zhang, A. Meijerink and M. Suta, One ion to catch them all: Targeted high-precision Boltzmann thermometry over a wide temperature range with Gd^{3+}, *Light: Sci. Appl.*, 2021, **10**, 236, DOI: **10.1038/s41377-021-00677-5**.

47 E. Song, M. Chen, Z. Chen, Y. Zhou, W. Zhou, H. T. Sun, X. Yang, J. Gan, S. Ye and Q. Zhang, Mn^{2+}-activated dual-wavelength emitting materials toward wearable optical fibre temperature sensor, *Nat. Commun.*, 2022, **13**, 2166, DOI: **10.1038/s41467-022-29881-6**.

48 M. K. Mahata, K. Kumar and V. K. Rai, Er^{3+}–Yb^{3+} doped vanadate nanocrystals: A highly sensitive thermographic phosphor and its optical nanoheater behavior, *Sens. Actuators, B*, 2015, **209**, 775–780, DOI: **10.1016/j.snb.2014.12.039**.

49 X. Cheng, K. Yang, J. Wang, L. Yang and X. Cheng, Upconversion luminescence and optical temperature sensing behaviour of Yb^{3+}/Er^{3+} codoped $CaWO_4$ material, *Opt. Mater.*, 2016, **58**, 449–453, DOI: **10.1016/j.optmat.2016.06.029**.

50 D. Chen, Z. Wan, Y. Zhou, X. Zhou, Y. Yu, J. Zhong, M. Ding and Z. Ji, Dual-phase glass ceramic structure, dual-modal luminescence and temperature sensing behaviors, *ACS Appl. Mater. Interfaces*, 2015, **7**, 19484–19493, DOI: **10.1021/acsami.5b06036**.

51 Y. Jiang, Y. Tong, S. Chen, W. Zhang, F. Hu, R. Wei and H. Guo, A three-mode self-referenced optical thermometry based on up-conversion luminescence of $Ca_2MgWO_6:Er^{3+},Yb^{3+}$ phosphors, *Chem. Eng. J.*, 2021, **413**, 127470, DOI: **10.1016/j.cej.2020.127470**.